Journal of The Electrochemical Society, **153** (7) A1372-A1377 (2006)
0013-4651/2006/153(7)/A1372/6/$20.00 © The Electrochemical Society

Microstructure Effects on the Electrochemical Kinetics of Vanadium Pentoxide Thin-Film Cathodes

Simon C. Mui,[a] Jacek Jasinski,[b] Valerie J. Leppert,[b] Masanori Mitome,[c] Donald R. Sadoway,[a,*] and Anne M. Mayes[a,*,z]

[a]*Department of Materials Science and Engineering, Massachusetts Institute of Technology, Cambridge, Massachusetts 02139-4307, USA*
[b]*School of Engineering, University of California at Merced, Merced, California 95344, USA*
[c]*Advanced Materials Laboratory, National Institute of Materials Science, 1-1 Namiki, Tsukuba, Ibaraki 305-0044, Japan*

The relationship between microstructure and electrochemical performance was investigated in sputter-deposited V_2O_5 thin-film cathodes. As-deposited and heat-treated films in unlithiated and lithiated states were studied by transmission electron microscopy, X-ray diffraction, and secondary ion mass spectroscopy. Film properties including orientation, grain size, and morphology were found to be strongly dependent on the heating rate during annealing. Large enhancements in the capacity–rate performance of coarser grained over nanocrystalline grained films were observed, contrary to expectations. Potential transient methods were used to investigate the mass-transport differences between these two distinct microstructures. Slow transport phenomena during phase transformation and interfacial impedances linked to differences in grain orientation and/or grain boundary content are proposed to explain the observed performance.
 [DOI: 10.1149/1.2199327]

Manuscript received January 17, 2006. Available electronically May 17, 2006.

New applications for power sources of micro- and nanoscopic dimensions have prompted integration of thin-film and semiconductor processing techniques to fabricate electrochemical storage devices.[1-3] Several lithium thin-film battery architectures with small footprints have been proposed for powering electronic devices such as remote sensors, implantable biomedical devices, Smartcards, microelectromechanical systems (MEMS) devices, and complementary metal oxide semiconductor (CMOS) memory.[4-7] The overall performance of miniaturized power sources is constrained by their architecture (i.e., cell design) and material properties (e.g., microstructure, composition, orientation). In thin-film batteries, the properties of the cathode as well as the cathode/electrolyte interface often dictate the kinetic limitations of the cell, making investigation into these areas germane.[8-12]

In particular, several groups have reported on the influence of the cathode film microstructure and orientation on electrochemical performance.[13-17] Film morphology, including grain size and distribution, shape, orientation, and crystallinity, can vary as a function of the deposition method, deposition parameters, choice of substrate, and postdeposition heat-treatment.[18-20] For instance, favorable orientations can enhance the electrochemical kinetics in layered compounds (e.g., $LiCoO_2$, V_2O_5, and $LiNiO_2$) owing to anisotropic diffusion in these systems.[16,17,21,22] Molecular dynamics simulations also have shown that both intergranular regions and grain orientation affect Li-ion transport.[23,24] Cocciantelli et al. reported lowered current-rate performance with larger, less favorably oriented V_2O_5 grains.[25] Their work suggests that sluggish diffusion can lead to partial phase transformation and the persistence of lithium-poor phases. Other studies have suggested that grain size, grain boundaries, and film stress can affect the electronic and ionic transport properties in ceramics.[26,27] While much of the literature has described the favorable effects of nanoscopic dimensions in composite electrodes,[13,28-33] nearly dense thin films can pose different structural challenges at the nanoscale.

In this study, the effects of thin-film microstructure on capacity-rate performance in radio-frequency-sputtered V_2O_5 films were investigated. The heating rate during annealing is shown to significantly affect microstructure, grain size, and orientation. An evaluation of diffusion coefficients and potential transient response curves is performed to understand performance differences between samples. X-ray diffraction (XRD) and transmission electron microscopy (TEM) analysis are also employed to understand the phase transformation process. Somewhat surprisingly, films possessing a coarse-grained microstructure exhibited superior rate capability to that of fine-grained films, which we attribute to differences in the kinetics of phase transformation between the two.

Experimental

Thin-film V_2O_5 cathodes were prepared by rf sputtering (CMS-18 deposition system, Kurt J. Lesker, Clairton, PA) onto aluminum foil (40 μm thick, 99% purity, annealed, Goodfellow Corp., Devon, PA). A 7.6 cm (3 in.) diam V_2O_5 target was prepared in-house by pressing and sintering V_2O_5 powder in air at 640°C. The target was subsequently bonded to a Cu backing plate using silver-loaded epoxy. V_2O_5 targets were sputtered at 250 W in an argon environment with 2 vol % oxygen. The latter reactive gas (99.97% purity Ar/O_2 mixture) was released through a gas ring surrounding the substrate. Typical sputtering rates were between 0.6–0.7 nm/min, particularly low because of the large substrate–target distance in the system (28 cm). The substrate was unheated. Thermocouples positioned near the substrate along with previous temperature calibrations indicated that the sample surface temperature remained below 150°C over the course of sputtering, well below the crystallization temperature for vanadium oxide.

Samples were allowed to cool in the chamber and were postannealed in air at 400°C for 1.5–24 h using Lindberg-Blue tube furnaces at heating rates ranging from 1 to 70°C/min. The vanadium oxide thickness was confirmed using surface profilometry (Tencor P-10) and cross-sectional scanning electron microscopy (JEOL 6320 field emission scanning electron microscope). Cross-sectional TEM specimens were prepared by means of mechanical prethinning and polishing, followed by Ar-ion milling. TEM studies were performed using a JEOL JEM-3010 operating at 300 kV and a JEOL JEM-2010 TEM operating at 200 kV accelerating voltage. Grain size was determined from cross-sectional micrographs, measuring the long and short dimensions of the grain, and averaging these values. Sample compositions, orientations, and lattice constants were determined using a Rigaku rotating anode X-ray diffractometer in Bragg–Brettano mode. Jade 7.0 analysis software was used for pattern refinement and peak fits (Materials Data, Inc.). Lattice parameters were obtained from a least-squares fit of six to eight reflections identified as vanadium pentoxide. Lithium-ion concentration profiles were determined by secondary ion mass spectroscopy (SIMS) performed on lithiated V_2O_5 films using a Cameca IMS-4f universal magnetic sector SIMS equipped with both oxygen and cesium ion

* Electrochemical Society Active Member.
z E-mail: amayes@mit.edu

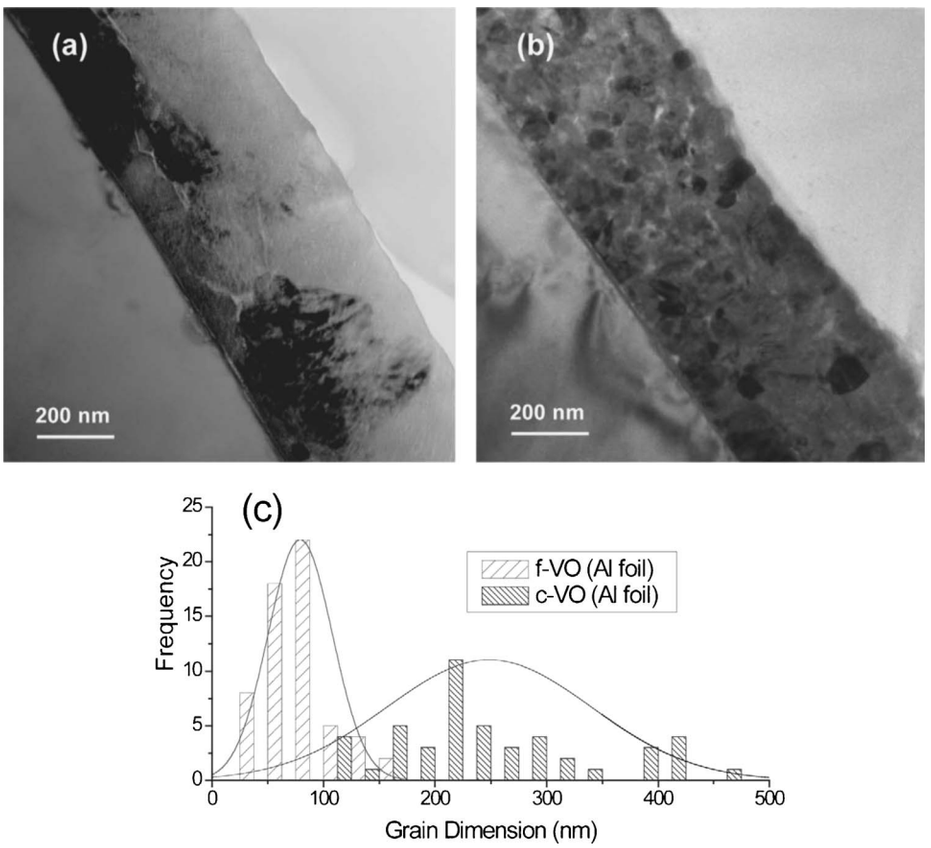

Figure 1. TEM micrographs of lithiated (a) c-VO and (b) f-VO (δ-phase $Li_xV_2O_5$ films, 3.08 V vs Li). Thickness of films ~500 nm. Scale bar equals 200 nm. (c) Grain size distribution of c-VO and f-VO films.

beams (Applied Microanalysis Labs, Santa Clara, CA). Films for the SIMS analysis were sputtered on indium tin oxide (ITO) substrates.

Electrochemical testing was performed in a two-electrode cell consisting of vanadium oxide (12 mm diam) as the working electrode and lithium metal (16 mm diam) as the counter/reference electrode. The electrolyte was a solution of 1 M $LiPF_6$ in ethylene carbonate/dimethyl carbonate (EC/DMC) (50:50 wt % Merck KGaA). Shorting of the electrodes was prevented by a microporous membrane spacer (Celgard 2300, Celgard, Inc.). Cells were assembled in an argon-filled glove box ((moisture <2 ppm), sealed, and tested at 25°C. Current-rate experiments, galvanostatic intermittent titration (GITT), and impedance spectroscopy were performed using Solartron 1286 and 1260 instruments in both coupled and stand-alone configurations. Over the potential range of the experiments (2.5–3.9 V vs Li) V_2O_5 exists in three crystal structures: α-$Li_xV_2O_5$ ($x \leqslant 0.1$), ε ($0.33 \leqslant x \leqslant 0.64$), and δ ($0.7 \leqslant x \leqslant 1$).[34,35] At 80% of the theoretical film density of 3.36 g/cm^3, $x = 0.90$ Li would correspond to a capacity of 35 μAh/μm cm^2. Discharge capacities at 1 μA/cm^2 were measured to be 35 ± 5 μAh/μm cm^2, the expected theoretical capacity accounting for experimental error.

Results and Discussion

Comparisons of electrochemical performance were made between samples from the same sputtering run to exclude batch-to-batch variations. Differences in microstructure and crystallite orientation were obtained by varying only one parameter, heating ramp rate, during the postanneal step. Figure 1 displays TEM cross-sectional images of as-sputtered, X-ray amorphous V_2O_5 thin films subsequently crystallized at a slow heating rate of 5°C/min (1a) and at a faster heating rate of 70°C/min (1b). Both sets of samples originated from the same sputtering run and are ~500 nm thick. The samples treated at a slower heating rate exhibit a coarser microstructure with grain sizes in the submicrometer range (110–470 nm, herein c-VO). Samples treated at a faster heating rate have a finer-grained microstructure with significantly smaller grains (30–170 nm, herein f-VO). A graph showing the grain size distribution is included in Fig. 1c. The mean grain size for f-VO is 80 ± 30 nm and for c-VO is 250 ± 90 nm.

Figure 2 shows the capacity-rate performance of c-VO and f-VO, along with that of the amorphous film prior to heat-treatment (non-HT). Heat-treatment of the amorphous as-deposited films resulted in a substantial enhancement of rate performance. Moreover, the rate performance of the c-VO samples (heated at a slower rate and hav-

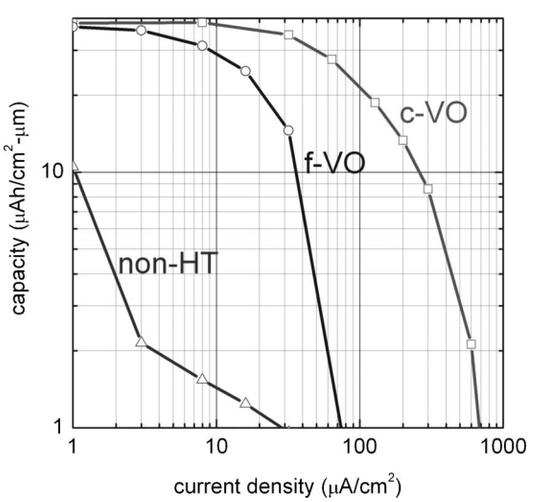

Figure 2. Capacity–rate plot (log–log) of V_2O_5 thin films as-deposited (non-HT), and annealed with a heating rate of 5°C/min (c-VO) and 70°C/min (f-VO).

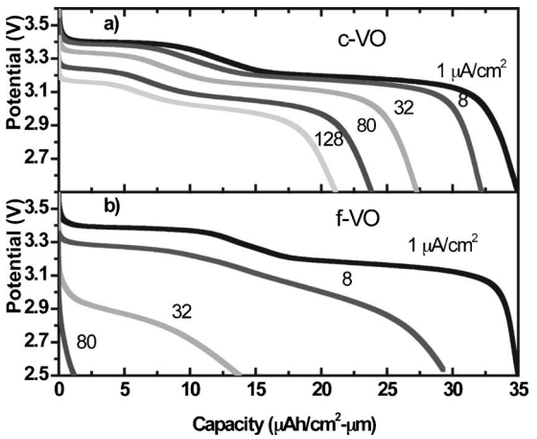

Figure 3. Discharge profiles of c-VO (5°C/min) and f-VO (70°C/min) for various current densities.

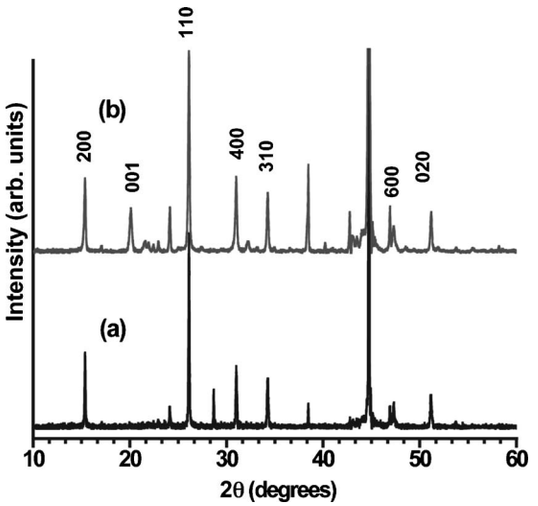

Figure 5. XRD patterns of (a) c-VO and (b) f-VO. The (110) peak intensities were normalized for pattern comparison.

ing a coarser grained microstructure) was found to be far superior to that of the f-VO samples. The curve for c-VO is observed to asymptote at current densities approaching 100 $\mu A/cm^2$, while f-VO asymptotes near 20 $\mu A/cm^2$. Figure 3a and b shows the galvanostatic discharge curves for c-VO and f-VO, respectively, at different current densities. The f-VO sample displays severe polarization at elevated currents, as well as the disappearance of discrete potential plateaus. The rapid reduction of capacity, along with the loss of distinct potential plateaus, is often associated with slow mass transport.[25,36]

Classical nucleation theory suggests that a slower heating rate would create smaller local thermal fluctuations, leading to fewer nucleation sites, more stable growth, and larger overall grain sizes.[37,38] Dark-field TEM images of these systems reveal wide grain boundaries of amorphous vanadium oxide (Fig. 4). Using the diffuse dark field technique for amorphous phase imaging, the grain boundary width was conservatively estimated to be 5 nm.[39-41] With the above values of grain size and grain boundary width, values of the grain boundary volume fraction were estimated to be ~4% for the c-VO sample and ~13% for the f-VO sample. Given these differences, the f-VO microstructure might be expected to enhance capacity-rate performance in thin films due to (*i*) enhanced diffusion along grain boundaries or (*ii*) reduced diffusion distances within grains as the result of electrolyte permeation through film microcracks or micropores. However, the opposite result is observed. The reasons for this apparent inconsistency are discussed below.

XRD patterns of sample films are compared in Fig. 5, with all peaks (marked) identified as V_2O_5 (PDF no. 41-1426) or from the aluminum substrate (unmarked). The space group describing δ-V_2O_5 is *Pmmn*(59), with reported lattice parameters of a_o = 11.5160, b_o = 3.5656, and c_o = 4.3727 Å.[42] The percentage of grains oriented with the (*hkl*) plane parallel to the substrate can be estimated by taking the ratio of the individual (*hkl*) peak area relative to the summed peak areas. The resulting distribution of orientations is given in Table I for each microstructure. Faster heating rates resulted in evolution of the (001) peak, denoting a greater percentage of grains with the [001] direction normal to the substrate. Differences in the orientations between f-VO and c-VO were observed in the (200), (001), and (110) peak intensities. The [001] direction represents a diffusion pathway perpendicular to the V–O layers, while the [200], [020], and [110] directions represent faster diffusion pathways between the layers. It is notable that moving to slow heating rates (c-VO) resulted in suppression of the (001)-oriented grains and an increase in the number of (110) and, to a smaller extent, the (200)-and (020)-oriented grains. The f-VO sample, with a larger percentage of (001) grains, would be expected to have slower initial intercalation of Li^+ ions into the film based on orientation.

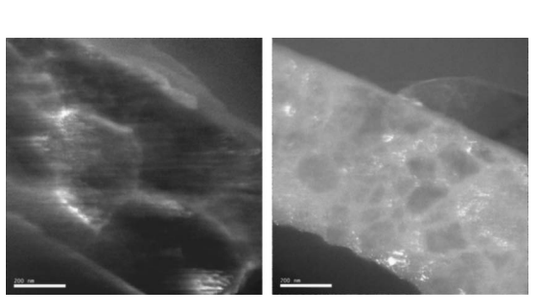

Figure 4. Dark-field TEM micrographs of c-VO (left) and f-VO (right), showing amorphous grain boundary regions. Scale bar equals 200 nm.

GITT was used to evaluate the diffusion coefficient of Li^+ as a function of degree of lithiation, following the approach first proposed by Weppner and Huggins.[43] A current pulse of 2.5 μA was applied for a period τ = 12 min. The voltage response was recorded. This was followed by a relaxation until the potential change was less than 5 mV over 1000 s. Under diffusion-controlled conditions, if $\tau \ll L^2/\tilde{D}$, where L is approximated as the thickness of the film, then the chemical diffusion coefficient can be represented by[43]

$$\tilde{D}_{\mathrm{GITT}} = \frac{4}{\pi}\left(\frac{V_M I_o}{SFz_i}\right)^2 \left[\frac{\left(\frac{dE_o}{d\delta}\right)}{\left(\frac{dE_p}{d\sqrt{t}}\right)}\right]^2 \qquad [1]$$

Here V_M is the molar volume, S the effective area, F the Faraday constant, z_i the moles of lithium involved in the electron-transfer reaction, I_o the current pulse magnitude, $dE_o/d\delta$ the slope of the steady-state voltage curve with lithium concentration, and $dE_p/d\sqrt{t}$

Table I. Percent grain orientations based on XRD peak intensities, c-VO and f-VO.

	(200), (400) (%)	(001) (%)	(110) (%)	(310) (%)	(020) (%)
c-VO	19.3	2.2	47.0	17.7	13.8
f-VO	17.5	19.9	39.0	12.4	11.3

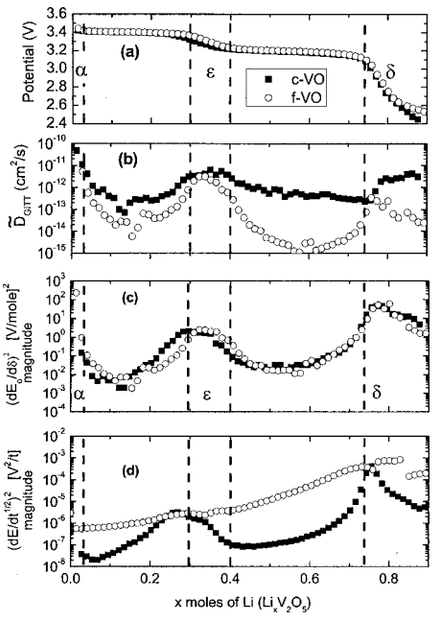

Figure 6. Variation in (a) steady-state voltage, (b) $\tilde{D}_{GITT}$, (c) $(dE_o/d\delta)^2$, and (d) $(dE_p/d\sqrt{t})^2$ with degree of lithiation as determined by GITT. The vertical lines delineate the α, ε, and δ regions. Values for $dE_o/d\delta$ and $\tilde{D}_{GITT}$ are undefined in the two-phase regions based on the derivation from Fick's law.

the slope of the transient voltage curve with the square root of time. A linear regression was performed to obtain the slope $dE_p/d\sqrt{t}$ for values of τ from 25–7200 s to ensure the initial iR drop was not included. Thus, the polarization results are attributed to the effects of mass transport within the film.

$\tilde{D}_{GITT}$ values, derived from Fick's law, implicitly assume a single-phase system. Consequently, for two-phase regions $\tilde{D}_{GITT}$ values are undefined. The single-phase regions are delineated in Fig. 6a and b, showing the steady-state voltage curve and the $\tilde{D}_{GITT}$ values. Note that the two-phase regions are shown only for completeness. In theory, if phase-boundary motion were assumed to be rapid, the chemical diffusion coefficient in the two-phase region would take on values between those of the single-phase end members.

The convergence in $\tilde{D}_{GITT}$ values over the α and ε single-phase regions for the two samples was unexpected, given the poor performance of f-VO relative to c-VO. To better understand the significance of $\tilde{D}_{GITT}$ values, a sensitivity analysis was performed upon Eq. 1 to determine whether the numerator $(dE_o/d\delta)^2$ or denominator $(dE_p/d\sqrt{t})^2$ dominates. It was found that over the potential range investigated, $\tilde{D}_{GITT}$ will be dominated in most cases by $(dE_o/d\delta)^2$ by more than an order of magnitude. This should be apparent because within the two-phase regions, over which the chemical potential is constant, the slope of the equilibrium potential curve approaches zero. Axiomatically, the $\tilde{D}_{GITT}$ values as determined by Eq. 1 will drop precipitously in two-phase regions, yielding results that are nonphysical.

Because a significant fraction of the capacity of vanadium oxide is found in two-phase regions, it would be constructive to have a valid metric to express the facility for mass transport and phase transformation over these ranges of composition while still utilizing experimental results obtained by the GITT method. It is proposed that the term $(dE_p/d\sqrt{t})^2$ can serve as such a metric. Figure 6 shows how the terms $(dE_o/d\delta)^2$ and $(dE_p/d\sqrt{t})^2$ from Eq. 1 vary with lithium concentration. The term $(dE_p/d\sqrt{t})^2$ represents the magnitude of the potential transient response and is reflective of mass-transport limitations together with differences in phase-transformation kinetics within the cathode. As expected, the slope of the steady-state curve (Fig. 6c) is nearly identical for c-VO and f-VO, while the potential transient response curve (Fig. 6d) varies significantly between the two systems. The f-VO, with smaller and more heavily (001)-oriented grains, responds more severely to current pulses over regions where phase transformation occurs. This response becomes even more pronounced at high degrees of lithiation. The severe transient responses shown by f-VO over the two-phase regions help explain its poorer rate capability compared to that of c-VO. These results suggest that rate limitations of the finer-grained film microstructure may primarily be attributed to less facile phase-transformation processes (i.e., two-phase regions).

Imperfections at the grain boundary regions can strongly influence transport properties and subsequent rate capability. As shown in Fig. 4, grain boundaries in both samples are amorphous and relatively broad ($\geqslant$5 nm).

Models of the amorphous grain boundary regions in V_2O_5 by Garofalini suggest that they can serve as high-diffusivity pathways for Li^+ movement.[24] However, from the perspective of Li^+ transport across grain boundaries, as likely here, amorphous intergranular regions might serve as additional high-resistance interfaces in series with faster bulk diffusion.[44,45] Jamnik generally found this to be the case when performing a circuit analysis on a polycrystalline, mixed-conductor system with semiblocking grain boundaries.[46] Notably, as-deposited amorphous films demonstrated poorer rate capability than either the coarse- or fine-grained crystalline systems (Fig. 2). It follows that the larger volume fraction of amorphous grain boundary regions present in the smaller grained films (Fig. 4) could significantly retard ion motion.

To further explore the differences in the rate of phase transformation between samples, XRD was used to evaluate the composition after slow and fast discharges to the ε + δ two-phase region. Slow mass transport (diffusion or phase boundary motion) would be expected to result in a higher concentration of the lithium-deficient phases (i.e., α and ε-$Li_xV_2O_5$). Two scenarios were devised to observe the ε → δ phase transformation. In case (I), the c-VO and f-VO were discharged at a low current density (3 μA/cm²) into the ε + δ two-phase region. The cutoff potential was fixed such that upon relaxation, the potential equilibrated to 3.18 V (surface concentration of $x \approx 0.6$, $Li_xV_2O_5$). In case (II), both samples were discharged at a higher current density (200 μA/cm²) into the ε + δ region and also allowed to reach an equilibrated potential of 3.18 V. Relative changes in the interlayer spacing, d_{001}, allowed for an estimate of the degree of transformation to the δ phase ($\sim Li_{0.9}V_2O_5$).[47]

Figure 7 shows the shift in the (001) peak position which is indicative of lithium insertion and phase transformation. At the low discharge rate, case (I), d_{001} has expanded by an average of 6.1% for c-VO and 4.2% for the f-VO sample. These results suggest that while the f-VO has a surface composition of $\sim Li_{0.6}V_2O_5$ during lithiation, the bulk of the film has not transformed to the extent observed in c-VO. This difference is magnified at the high discharge rate, case (II), where d_{001} expands by 5.8% for the c-VO but only by 1.9% for the f-VO. With a more favorable surface orientation and larger grains, c-VO may allow transformation within grains and phase boundary motion through the film to proceed more readily. The reduced layer expansion for f-VO suggests that the overall bulk composition was closer to $x \approx 0.1$–0.2 ($Li_xV_2O_5$) for the higher discharge rate and that a substantial fraction of α-phase still remains. An accurate quantification of the phase distribution was not possible due to the small sampling volume in the films (only an average change in d_{001} is reported). The multiphase coexistence was confirmed, however, by analysis of the (600) and (020) peaks, which exhibited some peak splitting (not shown).

The variation in Li^+ concentration with film depth was also mea-

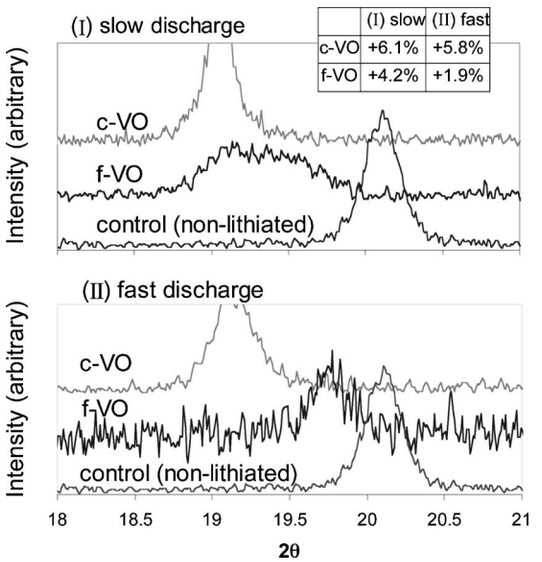

Figure 7. XRD of the (001) peak after samples were discharged at (I) 3 $\mu A/cm^2$ and (II) 200 $\mu A/cm^2$ and allowed to relax to 3.18 V vs lithium. The table in the upper right corner shows the average percent change in d_{001} as measured by the peak location.

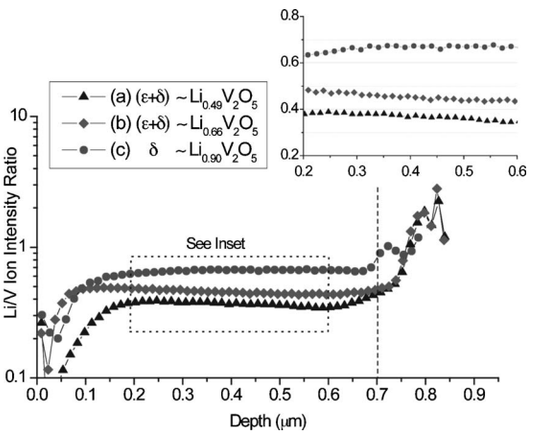

Figure 8. SIMS results showing Li/V concentration with depth for samples undergoing GITT and equilibration to the (a) beginning, (b) middle, and (c) end of the $\varepsilon \rightarrow \delta$ phase transformation. Dashed vertical line denotes the substrate.

sured by SIMS (Fig. 8). Three samples were galvanostatically titrated using a low discharge current of 1 $\mu A/cm^2$ to the (a) beginning, (b) middle, and (c) end of the $\varepsilon \rightarrow \delta$ phase transformation. To improve the accuracy of the measurements, the analysis was performed on films prepared on polished ITO/aluminosilicate substrates rather than Al foil. The grain orientation was largely similar to that of c-VO, as shown in Table II, but with smaller grain sizes (100–200 nm).

Sample (c), which was fully discharged to the δ phase, was used as a reference to compare against samples (a) and (b). The composition of $Li_{0.9}V_2O_5$ for sample (c) was estimated based on the electrochemical capacity and the potential discharge curve. The SIMS V/O intensity ratios were consistent between samples and uniform with depth. The estimated nominal compositions were calculated by integrating the ion intensities from the surface to the back of the films. For samples (a) and (b), the nominal compositions were $Li_{0.49}V_2O_5$ and $Li_{0.66}V_2O_5$, respectively. These values match reasonably well with those obtained from the electrochemical discharge, namely, (a) $Li_{0.55}V_2O_5$ and (b) $Li_{0.69}V_2O_5$.

The Li^+ concentration at the film surface was unexpectedly lower than in the film bulk. Part of the initial variation is due to surface roughness (~10–15 nm) and to the presence of a passive surface film formed from the electrolyte. The latter was detected by measuring the carbon concentration, which showed a layer of ~60 nm at the surface. Other effects, such as sample charging and material modifications caused by recoil implantation, may cause ion migration and make interpretation of Li^+ concentration profiles difficult.[48-50] Several experimental conditions were adjusted, including the use of a gold coating on the surface, application of an E-beam for charge neutralization, and use of the negative ion detection mode, to help reduce charging effects. However, the Li^+ depletion at the surface was still observed and appeared unchanged, regardless of experimental conditions.

Interestingly, Li^+ concentration diminishes linearly for films in the beginning (a) and middle (b) of the $\varepsilon \rightarrow \delta$ phase transformation, but remains constant for sample (c) in which the transformation is completed (Fig. 8, inset). The SIMS data suggest that phase boundary motion does not proceed as a planar front through the film. Otherwise, one might expect a sharp drop in lithium concentration with depth as the film is converted from ε to δ (absent substantial SIMS-induced migration within the film bulk). Instead, a slight linear decrease is observed for samples (a) and (b), a result suggesting that the ratio of c_δ/c_ε (delta/epsilon phase concentration) is on average decreasing with depth into the sample. By contrast, the single-phase δ sample (c) has a more uniform Li^+ concentration with depth, as would be expected. The SIMS analysis indicating that phase boundary penetration is variable throughout the film rather than uniform is consistent with TEM studies by Iriyama et al. of the two-phase region in another layered compound, Li_xMoO_3 ($0 \leqslant x \leqslant 0.3$), which revealed that the insertion process proceeded inhomogeneously, with some grains becoming lithiated preferentially while other neighboring grains remained unlithiated until further into the discharge.[51]

In addition to differences in mass transport between c-VO and f-VO, interfacial effects were also considered. The initial iR drop during GITT measurements was used as a measure of the polarization corresponding to the summation of electrolyte, interface, and electronic resistances in the cathode and cell. Values for R_{GITT} ranged from 6 to 11 kΩ for c-VO and 11 to 17 kΩ for f-VO over the lithiation range. For both samples, R_{GITT} increases rapidly with increasing lithiation (not shown). Impedance spectroscopy and further polarization analysis were used to better understand trends in these results. Different crystal habits at the surface may be expected to exhibit differing electrode–electrolyte interactions (e.g., adsorption, defect sites, surface charge). Although well-matching equivalent circuits were not found due to the complexity of the system, impedance results showed the more randomly oriented f-VO had higher resistances associated with the interface (34 vs 11 $k\Omega\ cm^2$), as shown in Fig. 9. This may possibly be due to differences in grain orientation or grain boundary fraction at the surface, or surface roughness associated with the smaller grain sizes.

An analysis of the polarization that occurred during galvanostatic testing also supported the impedance and R_{GITT} results. The potentials of the $\alpha + \varepsilon$ and $\varepsilon + \delta$ plateaus were identified by taking the differential of the capacity vs potential (dQ/dE). Resistance values

Table II. Percent grain orientations based on XRD peak intensities, V_2O_5 on ITO.

	(200), (400) (%)	(001) (%)	(110), (220) (%)	(310) (%)	(020) (%)
V_2O_5/ITO	18.2	0.0	51.3	15.7	14.7

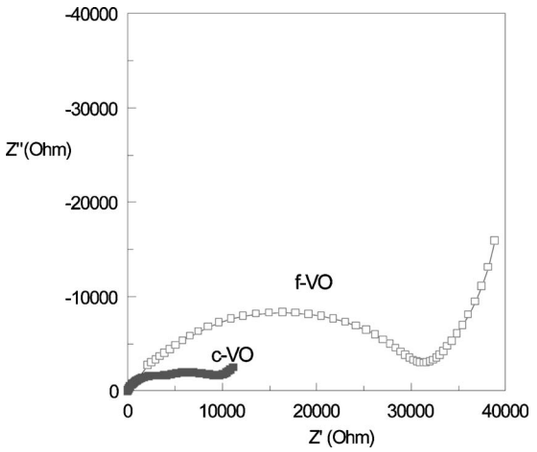

Figure 9. Impedance spectra of (■) c-VO and (□) f-VO at 3.35 V vs Li.

were calculated by measuring the polarization of these differential peaks (dQ/dE). The c-VO sample was found to have resistances, R_η, of roughly 1.3 and 1.7 kΩ for the $\alpha \rightarrow \varepsilon$ and $\varepsilon \rightarrow \delta$ reaction, respectively, while for f-VO these values were $R_\eta \approx 14$ and 24 kΩ. These resistances represent the summation of both activation and bulk concentration polarization. The three results ascertained from evaluating the iR from the GITT data, impedance plots, and the differential capacity all suggest that interfacial resistance is larger in the samples having greater percentage (001) orientation and smaller crystallites. At current densities approaching 100 $\mu A/cm^2$, the degree of polarization is severe (>0.5 V), with interfacial resistances greater than 5 kΩ. These polarizations lead to greater suppression of the potential plateaus in f-VO compared with c-VO.

Conclusion

It was found that phase transformation kinetics can limit the current-rate performance in thin-film V_2O_5 cathodes. In contrast to the expectations from previous models, a fine-grained film performed substantially worse than a coarse-grained film.[24,52,53] Differences in grain orientation and/or grain boundary content appear to affect phase-boundary mobility through the film. The term $(dE_p/d\sqrt{t})^2$ provided a metric to assess the degree of polarization during the phase-transformation process and effective limitations due to both diffusion and phase boundary motion. Combined SIMS and XRD results suggest that the phase transformation may proceed in an inhomogeneous fashion through the film rather than as a uniform, planar front. Interfacial resistance was also measured to be significantly larger for the fine-grained films.

Acknowledgments

The authors acknowledge Elsa A. Olivetti for her assistance with elemental analysis of the films. This work was supported in part by the MRSEC Program of the National Science Foundation under award number DMR-0213282 and by the Office of Naval Research under grant numbers N00014-02-1-0226 and N00014-05-0056. TEM studies were supported by the National Science Foundation under award number DMR-0137922 and the International Center for Young Scientists, National Institute for Materials Science, Tsukuba, Japan, under MEXT. The National Center for Electron Microscopy at Lawrence Berkeley National Laboratory under the U.S. Department of Energy contract DE-AC-03-76SF00098 and the Imaging and Microscopy Facility at the University of California, Merced, are gratefully acknowledged for use of their instruments.

Massachusetts Institute of Technology assisted in meeting the publication costs of this article.

References

1. S. H. Lee, P. Liu, C. E. Tracy, and D. K. Benson, *Electrochem. Solid-State Lett.*, **2**, 425 (1999).
2. K. Kanehori, K. Matsumoto, K. Miyauchi, and T. Kudo, *Solid State Ionics*, **9–10**, 1445 (1983).
3. D. Singh, R. Houriet, R. Giovannini, H. Hofmann, V. Cracium, and R. K. Singh, *J. Power Sources*, **97–8**, 826 (2001).
4. B. Scrosati, G. B. Appetecchi, F. Croce, S. Panero, and S. Passerini, Abstract 578, p. 925, *The Electrochemical Society Meeting Abstracts*, Vol. 96-1, Chicago, IL, Oct. 8–13, 1995.
5. J. B. Bates, N. J. Dudney, B. Neudecker, A. Ueda, and C. D. Evans, *Solid State Ionics, Diffus., React.*, **135**, 33 (2000).
6. C. Julien, M. A. Camacho Lopez, L. Escobar Alarcon, and E. Haro Poniatowski, *Mater. Chem. Phys.*, **68**, 210 (2001).
7. M. Z. A. Munshi and B. B. Owens, *Solid State Ionics, Diffus., React.*, **38**, 103 (1990).
8. G. G. Botte, V. R. Subramanian, and R. E. White, *Electrochim. Acta*, **45**, 2595 (2000).
9. J. B. Goodenough, *Solid State Ionics*, **69**, 184 (1994).
10. M. V. Mirkin, F. R. F. Fan, and A. J. Bard, *Science*, **257**, 364 (1992).
11. J. Bates, G. Gruzalski, N. Dudney, C. Luck, and X. Yu, *Solid State Ionics*, **70–71**, 619 (1994).
12. N. J. Dudney and Y. I. Jang, *J. Power Sources*, **119–121**, 300 (2003).
13. E. Antolini, *Solid State Ionics*, **170**, 159 (2004).
14. M. Deepa, A. K. Srivastava, S. Singh, and S. A. Agnihotry, *J. Mater. Res.*, **19**, 2576 (2004).
15. H. Miyazaki, H. Sakamura, M. Kamei, and I. Yasui, *Solid State Ionics*, **122**, 223 (1999).
16. J. B. Bates, N. J. Dudney, B. J. Neudecker, F. X. Hart, H. P. Jun, and S. A. Hackney, *J. Electrochem. Soc.*, **147**, 59 (2000).
17. P. J. Bouwman, B. A. Boukamp, H. J. M. Bouwmeester, and P. H. L. Notten, *Solid State Ionics*, **152**, 181 (2002).
18. J. A. Thornton, *J. Vac. Sci. Technol. A*, **4**, 3059 (1986).
19. C. R. Aita, *J. Vac. Sci. Technol. A*, **11**, 1540 (1993).
20. B. A. Movchan and A. V. Demchishin, *Phys. Met. Metallogr.*, **28**, 83 (1969).
21. P. J. Bouwman, B. A. Boukamp, H. J. M. Bouwmeester, and P. H. L. Notten, *J. Electrochem. Soc.*, **149**, A699 (2002).
22. C. Navone, R. Baddour-Hadjean, J. P. Pereira-Ramos, and R. Salot, *J. Electrochem. Soc.*, **152**, A1790 (2005).
23. M. E. Garcia and S. H. Garofalini, *J. Electrochem. Soc.*, **146**, 840 (1999).
24. S. H. Garofalini, *J. Power Sources*, **110**, 412 (2002).
25. J. M. Cocciantelli, M. Menetrier, C. Delmas, J. P. Doumerc, M. Pouchard, M. Broussely, and J. Labat, *Solid State Ionics*, **78**, 143 (1995).
26. J. F. Whitacre, W. C. West, E. Brandon, and B. V. Ratnakumar, *J. Electrochem. Soc.*, **148**, A1078 (2001).
27. P. Heitjans and S. Indris, *J. Phys.: Condens. Matter*, **15**, R1257 (2003).
28. P. Heitjans and S. Indris, *J. Mater. Sci.*, **39**, 5091 (2004).
29. M. Ulrich, A. Bunde, S. Indris, and P. Heitjans, *Phys. Chem. Chem. Phys.*, **6**, 3680 (2004).
30. K. F. Hsu, S. Y. Tsay, and B. J. Hwang, *J. Mater. Chem.*, **14**, 2690 (2004).
31. M. Nakayama, K. Watanabe, H. Ikuta, Y. Uchimoto, and M. Wakihara, *Solid State Ionics*, **164**, 35 (2003).
32. J. S. Sakamoto, C. K. Huang, S. Surampudi, M. Smart, and J. Wolfenstine, *Mater. Lett.*, **33**, 327 (1998).
33. M. Kalbac, M. Zukalova, and L. Kavan, *J. Solid State Electrochem.*, **8**, 2 (2003).
34. C. Satto, P. Sciau, E. Dooryhee, J. Galy, and P. Millet, *J. Solid State Chem.*, **146**, 103 (1999).
35. D. W. Murphy, P. A. Christian, F. J. Disalvo, and J. V. Waszczak, *Inorg. Chem.*, **18**, 2800 (1979).
36. P. Arora, M. Doyle, A. S. Gozdz, R. E. White, and J. Newman, *J. Power Sources*, **88**, 219 (2000).
37. S. E. Offerman, N. H. Van Dijk, J. Sietsma, E. M. Lauridsen, L. Margulies, S. Grigull, H. F. Poulsen, and S. Van Der Zwaag, *Acta Mater.*, **52**, 4757 (2004).
38. J. W. Christian, *The Theory of Transformations in Metals and Alloys*, Pergamon Press, Elmsford, NY (1981).
39. D. R. Clarke, *J. Am. Ceram. Soc.*, **70**, 15 (1987).
40. D. R. Clarke, *Ultramicroscopy*, **4**, 33 (1979).
41. M. K. Cinibulk, H. J. Kleebe, and M. Ruhle, *J. Am. Ceram. Soc.*, **76**, 426 (1993).
42. Powder Diffraction Standards File No. 41-1426.
43. W. Weppner and R. A. Huggins, *J. Electrochem. Soc.*, **124**, 1569 (1977).
44. A. Atkinson, *Surf. Interfaces Ceram. Mater.*, **1989**, 273.
45. J. Jamnik and J. Maier, *Phys. Chem. Chem. Phys.*, **5**, 5215 (2003).
46. J. Jamnik, *Solid State Ionics*, **157**, 19 (2003).
47. J. M. Cocciantelli, J. P. Doumerc, M. Pouchard, M. Broussely, and J. Labat, *J. Power Sources*, **34**, 103 (1991).
48. A. Benninghoven, F. G. Rüdenauer, and H. W. Werner, *Secondary Ion Mass Spectroscopy: Basic Concepts, Instrumental Aspects, Applications, and Trends*, Wiley, New York (1987).
49. M. Shaanan and R. Kalish, *Nucl. Instrum. Methods Phys. Res. B*, **171**, 332 (2000).
50. P. N. K. Deenapanray and M. Petravic, *J. Appl. Phys.*, **87**, 2178 (2000).
51. Y. Iriyama, T. Abe, M. Inaba, and Z. Ogumi, *Solid State Ionics*, **135**, 95 (2000).
52. J. H. Harding, *Interface Sci.*, **11**, 81 (2003).
53. I. Kaur and W. Gust, *Fundamentals of Grain and Interphase Boundary Diffusion*, Ziegler Press, Stuttgart (1989).